



Three-dimensional Core@Shell Co@CoMoO₄ nanowire arrays as efficient alkaline hydrogen evolution electro-catalysts

Rui Xiang, Yijun Duan, Lishan Peng, Yao Wang, Cheng Tong, Ling Zhang, Zidong Wei*

Chongqing Key Laboratory of Chemical Process for Clean Energy and Resource Utilization, School of Chemistry and Chemical Engineering, Chongqing University, Chongqing, 400044, China



ARTICLE INFO

Keywords:

Hydrogen evolution reaction
Electro-catalysis
Nanowire arrays
Interface engineering
Molybdate

ABSTRACT

Tailoring efficient and stable electrocatalysts based on non-noble metal elements for hydrogen evolution reaction (HER) is highly imperative for the commercialization of water splitting electrolyzers. Herein, a self-standing core@shell Co@CoMoO₄ nanowire array (Co@CoMoO₄ NA) electrode is developed by calcination of a cobalt carbonate hydroxide@CoMoO₄ (CCH NA@CoMoO₄) precursor under H₂/N₂ atmosphere. In this way, synergistic Co/CoMoO₄ heterostructure interfaces and 3D porous electrode architecture are built up, which are proved to be reliable strategies for HER catalytic activity enhancement. In 1.0 M KOH solution, Co@CoMoO₄ NA electrode exhibits an impressive activity with an extremely low overpotential of 46 mV at 10 mA cm⁻², quite closing to that of commercial PtC (31 mV at 10 mA cm⁻²). These findings may inspire the exploration of new electro-catalysts for efficient HER by modulating multiple components interfaces.

1. Introduction

Molecular hydrogen has been suggested as a promising alternative for the future energy supply, owing to its highest gravimetric energy density compared with other fuels and environmental benignity with water as the only combustion product [1,2]. Currently, the mass production of H₂ is mostly relied on steam methane reforming and coal gasification rather than electrolysis of water, although the latter strategy is beneficial for a number of advantages (e.g. using water as starting material, no greenhouse gases emission and high purity product) [3–6]. One of the main obstacles for large scale electrochemical splitting of water is the lack of efficient and stable hydrogen evolution reaction (HER) catalysts [7]. Platinum (Pt) is the most active and durable HER catalyst, however, its high cost and scarce greatly hinders its widespread applications [8]. Therefore, it is highly imperative for the development of noble metal-free electro-catalysts in the perspective of commercialization of water splitting electrolyzers.

During the past decades, various earth abundant materials have been proved to be capable of catalyzing HER in alkaline media, including transition-metal carbides [9–11], phosphides [12], chalcogenides [13–16], metal alloys [17–19] and so on [3,20]. Among them, Co-based materials such as O-Co₂P-3 [21], P_{8.6}-Co₃O₄/NF [22], Co(OH)₂@NCNTs@NF [23], Co₃Se₄/CF [24], CP/CTs/Co-S [25], CoMoO₄ NWA/Ti [26], etc. have been intensively studied as HER electro-catalysts,

owing to elemental abundance, diversity and theoretically high catalytic activity [27,28]. However, the experimental performance of these materials is generally far from satisfactory. Therefore, several studies have payed attention to the construction of multiple components interfaces for taking advantage of synergistic effects between the individual components [29–31]. For example, with CoO/MoO_x derived from high-temperature hydrogenation treatment of CoMoO₄ precursor, overpotential of 163 mV afforded the benchmark current density of 10 mA cm⁻² in 1.0 M KOH solution [32]. Nevertheless, the observed performance of CoO/MoO_x is far behind that of MoNi₄/MoO_{3-x} (17 mV at 10 mA cm⁻²) derived from a similar hydrogenation treatment process with NiMoO₄ as precursor [33]. In addition, another drawback for traditional hydrogenation strategy with a single compound (CoMoO₄) as precursor is that the density of interface area can hardly be tuned, as the Co/Mo ratio in CoMoO₄ is constant of 1:1. Inspired by the adjacent position of Ni and Co in the volcano plot for HER (i.e. a similar moderate H-bonding energy) [34], we speculate that highly efficient HER catalysts can be synthesized by tailoring the interfaces between Co and Mo compounds. On the other hand, introduction of vacancy sites has also been proved to be a useful strategy for tailoring the HER performance [35,36], as additional active sites can be created or the kinetics energy barrier can be optimized [37]. Therefore, combination of interfacial engineering with intentional introduced vacancies should be beneficial to the construction of low-cost efficient HER catalysts.

* Corresponding author.

E-mail address: zdwei@cqu.edu.cn (Z. Wei).

Based on the above analysis, herein, we report the preparation of self-standing Co@CoMoO₄ NA on Ni foam as an efficient and durable integrate HER electrode. The synthesis procedure involves the first construction of cobalt carbonate hydroxide nanowire arrays (CCH NA), and then the deposition of an amorphous CoMoO₄ shell by chemical bath deposition (CBD). Finally, hydrogenation treatment of the resultant precursor led to core@shell Co@CoMoO₄ NA. Benefiting from several advantage aspects, such as successful construction of Co/CoMoO₄ interfaces, open porous structure and intimate contact with conductive substrate, the entitled electrode demonstrates greatly enhanced HER activity. In 1.0 M KOH solution, overpotential of 46 mV afforded a current density of 10 mA cm⁻², which is quite close to that of commercial PtC (31 mV at 10 mA cm⁻²).

2. Experimental

2.1. Material preparation

2.1.1. Cobalt carbonate hydroxide nanowire arrays (CCH NA)

The synthesis procedure follows the published paper with modification [38,39]. Specifically, a 2 × 4 cm² Ni foam was immersed into 3 M HCl solution under sonication for 10 min, and then washed with ethanol and ultrapure water successively under sonication for 10 min A hydrothermal reaction solution was prepared by adding 1.019 g Co (NO₃)₂·6H₂O and 1.051 g CO(NH₂)₂ into 35 mL H₂O. After stirring for 15 min, the above solution and the pretreated Ni foam was transferred into an autoclave. Hydrothermal reaction was conducted at 120 °C for 10 h. After cooling to room temperature naturally, the obtained product was washed thoroughly with ultrapure water under sonication and dried in an electronic oven at 60 °C.

2.1.2. cobalt carbonate hydroxide@CoMoO₄ nanowire arrays (CCH NA@CoMoO₄)

A chemical bath deposition (CBD) method was adopted. Briefly, a chemical bath deposition solution contains 20 mM Co(NO₃)₂·6H₂O and 20 mM Na₂MoO₄·2H₂O was prepared. The as obtained CCH NA on Ni foam was then immersed into the above-mentioned CBD solution. Then, CBD reaction was conducted with a 75 °C water bath for 30 min unless otherwise stated. Finally, the Ni foam loaded with CCH NA@CoMoO₄ was washed with pure water and dried in an electronic oven at 60 °C.

2.1.3. Co@CoMoO₄ nanowire arrays (Co@CoMoO₄ NA) and Co nanowire arrays (Co NA)

The as obtained CCH NA@CoMoO₄ precursor was heated at different temperatures (300 °C, 400 °C, 500 °C) for 30 min in a tube furnace under H₂/N₂ (10:90) atmosphere with a heating rate of 5 °C/min to synthesis Co@CoMoO₄ NA. As a control, CCH NA was annealed with the same protocol as stated above to obtain Co NA.

2.1.4. CoMoO₄ nanosheet arrays

Preparation of CoMoO₄ follows the published hydrothermal route with modification [40]. Ni foam (1 × 4 cm²) was pretreated following the above stated procedure. A solution was prepared by adding 1.5 mmol Co(NO₃)₂·6H₂O and 1.5 mmol Na₂MoO₄·2H₂O into 30 mL ethanol aqueous solution (V (ethanol): V (H₂O) = 1:1) under vigorous stirring for 30 min. Then Ni foam and the reaction solution were transferred into an autoclave. Hydrothermal reaction was conducted at 160 °C for 4 h. After cooling to room temperature naturally, as obtained Ni foam was washed with water under sonication, and then dried in an electronic oven at 60 °C. Finally, the resultant Ni foam loaded with CoMoO₄ was heated for 30 min in a tube furnace under H₂/N₂ (10:90) atmosphere with a heating rate of 5 °C/min.

2.1.5. PtC electrode

2 mg commercial PtC 20 wt.% was dispersed into a mixture solution of 800 μL Milli-Q water, 190 μL isopropanol and 10 μL 5 wt.% Nafion.

After sonication of 30 min, 500 μL of the above-stated catalyst ink was casted onto 1 × 1 cm² pretreated Ni foam.

2.2. General characterizations

The surface morphology and the microstructure of the catalysts were analyzed by X-ray diffraction (XRD-6000, Shimadzu), X-ray photoelectron spectroscopy (XPS, PHI 550 ESCA/SAM), field-emission scanning electron microscopy (FE-SEM, JSM-7800, Japan), and energy dispersive X-ray spectra (EDS, OXFORD Link-ISIS-300), respectively. Transmission electron microscopy (TEM) measurements were tested on a Hitachi H-8100 electron microscope (Hitachi, Tokyo, Japan) with an accelerating voltage of 200 kV. Temperature programmed reduction (H₂-TPR) were tested by a HUASI DAS-7000 automatic analyzer. 50.0 mg of a catalyst was firstly placed in a U-tube quartz reactor, heated in 30 sccm stream of He to 300 °C and kept for 1 h to outgas the sample. The sample was then cooled down to 50 °C in He, then switched to 5.0% H₂/Ar. The sample temperature was then increased to 900 °C at a heating rate of 10 °C /min.

2.3. Electrochemical measurements

Electrochemical measurements were conducted by a Princeton Applied Research Parstat 4000 potentiostat at room temperature. A standard three-electrode system was used. The as synthesized electrodes were directly used as working electrode, and a carbon rod was used as counter electrode. A double-bridged Ag/AgCl (3 M KCl) was used as reference electrode and calibrated in high purity H₂ saturated 1.0 M KOH solution with a Pt wire as the working electrode. Unless otherwise stated, potentials were converted to overpotential (η) according to equations: $\eta = E$ (vs. RHE) - 0 V; E (vs. RHE) = E (vs. Ag/AgCl) + 1.016 V. Prior to data collection, 20 cycles of cyclic voltammetry (CV) was conducted between 0.2 ~ -0.2 V (vs. RHE). Linear sweep voltammetry (LSV) was recorded without iR correction at a scan rate of 1 mV s⁻¹ between 0.2 ~ -0.5 V (vs. RHE). AC impedance measurements were carried out at overpotential of 50 mV between frequency ranges from 10 kHz to 0.01 Hz. The data was analyzed and fitted using ZSimpWin software. For the determination of double layer capacitance (C_{dl}), CV scans between 0.1 ~ 0.15 V (vs. RHE) were conducted at 4, 6, 8, 10 and 12 mV s⁻¹. To test stability, chronopotentiometry method was conducted at fixed current for 20 h. Faraday efficiency was measured with a home-made water gas displacement system, and a constant current density of 30 mA cm⁻² was imposed.

3. Results and discussion

3.1. Material preparation and characterization

The preparation procedure of Co@CoMoO₄ NA is schematically illustrated in Fig. 1. Commercial Ni foam is selected as a conductive substrate, owing to its 3D macro-porous structure and low cost. Firstly, cobalt carbonate hydroxide nanowire arrays (CCH NA) are grown on Ni foam by a well-developed hydrothermal route. Then, a chemical bath deposition (CBD) process is conducted as the second step to decorate CoMoO₄ species on the surface of CCH NA. Finally, heating at 400 °C in H₂/N₂ (10:90) atmosphere results in the reduction of CCH NA@-CoMoO₄ to Co@CoMoO₄ NA.

X-ray diffraction (XRD) characterization was conducted to check the phase evolution. As shown in Fig. 2a, with a facile hydrothermal route, the obtained CCH NA precursor with diffraction peaks at 17.5°, 26.7°, 33.8°, 35.4°, 39.5°, 47.3° can be indexed to phase pure cobalt carbonate hydroxide hydrate (Co(CO₃)_{0.5}(OH)·0.11H₂O, JCPDS No. 48-0083). After CBD treatment, no prominent changes were recorded by XRD measurements, indicating the amorphous nature of the chemical bath deposited CoMoO₄. The final product obtained by calcination in H₂/N₂ atmosphere was also tested by XRD, and the recorded signals

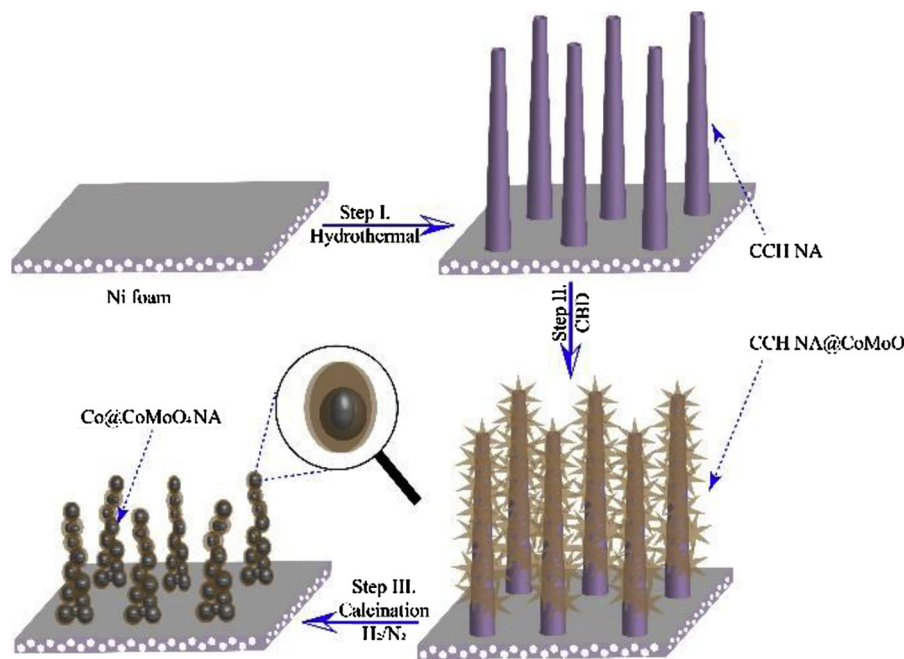


Fig. 1. Schematic illustration of the preparation procedure for Co@CoMoO₄ NA.

correspond to diffractions from (111), (200) and (220) planes of cobalt (JCPDS No. 15-0806). The surface chemical features of Co@CoMoO₄ NA were probed by X-ray photoelectron spectroscopy (XPS). As shown in Figure S1, survey spectrum of Co@CoMoO₄ NA reveals the coexistence of Co, Mo, O and C elements. The high-resolution Co 2p and Mo 3d spectra are illustrated in Fig. 2b and c. The Co 2p core-level spectra of Co@CoMoO₄ NA demonstrate two prominent peaks at binding energies (BE) of 780.8 eV and 796.9 eV, which could be indexed to Co 2p_{3/2} and Co 2p_{1/2} as characteristics of Co²⁺ [26,41,42]. Mo 3d core-level spectra in Fig. 2c shows two signals at binding energies of 232.5 eV and 235.6 eV, belonging to 3d_{5/2} and 3d_{3/2} of Mo⁶⁺ in MoO₄²⁻, respectively [43]. In addition, a minor Mo⁵⁺ species (Atomic % = 7.1%) was detected at lower binding energies of 230.6 eV (Mo 3d_{5/2}) and 232.6 eV (Mo 3d_{3/2}) [44]. The O 1s spectra (Fig. 2d) show one peak at BE of 530.3 eV corresponding to the lattice O²⁻ in CoMoO₄, and another peak at BE of 531.2 eV belonging to O-vacancies [45,46]. The above results demonstrate that metallic Co core with amorphous CoMoO₄ shell was obtained through the proposed synthetic approach.

Scanning electron microscopy (SEM) reveals the morphology characters. As shown in Fig. 3a1 and a2, numerous needles-like nanowires perpendicular to the substrate are observed after hydrothermal reaction. With a CBD process, irregular nanosheets are decorated on the surface of these needles-like nanowires (Fig. 3b1, b2 and Figure S2a), forming a core-shell structure. Subsequent calcination under H₂/N₂ atmosphere makes these nanowires shrink, and converts to highly porous nanowire arrays (Fig. 3c1, c2 and Figure S2b). The surface area will be greatly increased by this electrode design, providing more electroactive sites for HER. In such an ordered nanowire array structure, the open space between the core/shell nanowire arrays can be efficiently utilized, ensuring an easy diffusion of electrolyte ions and dissipation of hydrogen bubbles. The decoration of CoMoO₄ shell by CBD on the surface of CCH NA plays a significant role for Co@CoMoO₄ NA to retain the overall nanowire array morphology. As depicted in Figure S3, irregular, highly shrinkage and fused structure was observed by annealing CCH NA with the same protocol as that of Co@CoMoO₄ NA (See experimental), demonstrating that the fusion of Co during hydrogenation treatment was greatly hindered by the outward CoMoO₄ shell. Transmission Electron Microscopy (TEM) further reveals the detailed morphology and composition characters. As shown in Fig. 4a, b

and c, the as-obtained porous nanowires are actually composed of numerous nanoparticles with numerous voids. In addition, a distinct surface layer surrounding the nanoparticles with lower contrast is observed (Fig. 4b, c), clearly indicating a core-shell structure of the resultant Co@CoMoO₄ NA. High-resolution TEM image shows clear interface between Co core and CoMoO₄ shell (Fig. 4d). Moreover, as shown in the inset of Fig. 4d, interplanar spacing of 0.204 nm and 0.175 nm are respectively assigned to the (111) and (200) lattice planes of cubic cobalt. Consistent with the XRD results, the CoMoO₄ shell existed mostly as amorphous phase, since only sporadic domains with blurry lattice fringes can be found (Fig. 4d and e). The selected-area diffraction (SAED) pattern for Co@CoMoO₄ NA in Fig. 4f reveals clear diffraction rings, and each diffraction ring is also well indexed to cubic cobalt. TEM elemental mapping (Fig. 4g-k) of Co@CoMoO₄ NA reveals the uneven distribution of Co and Mo elements, indicating a Co rich core and Mo rich shell. Therefore, all the above results undoubtedly suggest the successful construction of core@shell Co@CoMoO₄ nanowire arrays.

3.2. HER performance

The HER catalytic activity of the as-prepared Co@CoMoO₄ NA electrode was directly elucidated as a binder-free integrate electrode with a standard three-electrode system in 1.0 M KOH. Bare Ni foam, 20% PtC, Co NA and CoMoO₄ were also tested for comparison. In order to avoid any contaminant originated from Pt, a graphite rod was used as the counter electrode. The polarization curves were firstly recorded without ir compensation. As depicted in Fig. 5a, dramatically enhanced HER catalytic currents are observed for Co@CoMoO₄ NA, but bare Ni foam shows a negligible current. To reach the benchmark current density of 10 mA cm⁻², Co@CoMoO₄ NA only needs a small overpotential of 46 mV, far less than that of bare Ni foam (265 mV). Although the observed catalytic activity of Co@CoMoO₄ NA is slightly inferior to commercial PtC (31 mV at 10 mA cm⁻²), it is among the best non-precious metal based HER catalysts and superior to most recently reported Co based HER catalysts such as P_{8.6}-Co₃O₄/NF (η_{10} = 97 mV) [22], amorphous CoMoO₄ NWA/Ti (η_{10} = 81 mV) [26], TiO₂ NDs/Co NSNTs-CFs (η_{10} = 108 mV) [47], Co/Co₃O₄ (η_{20} = 129 mV) [45], ECA-CoNPs@C (η_{10} = 58 mV) [48] (See more details in Table S1). Co NA

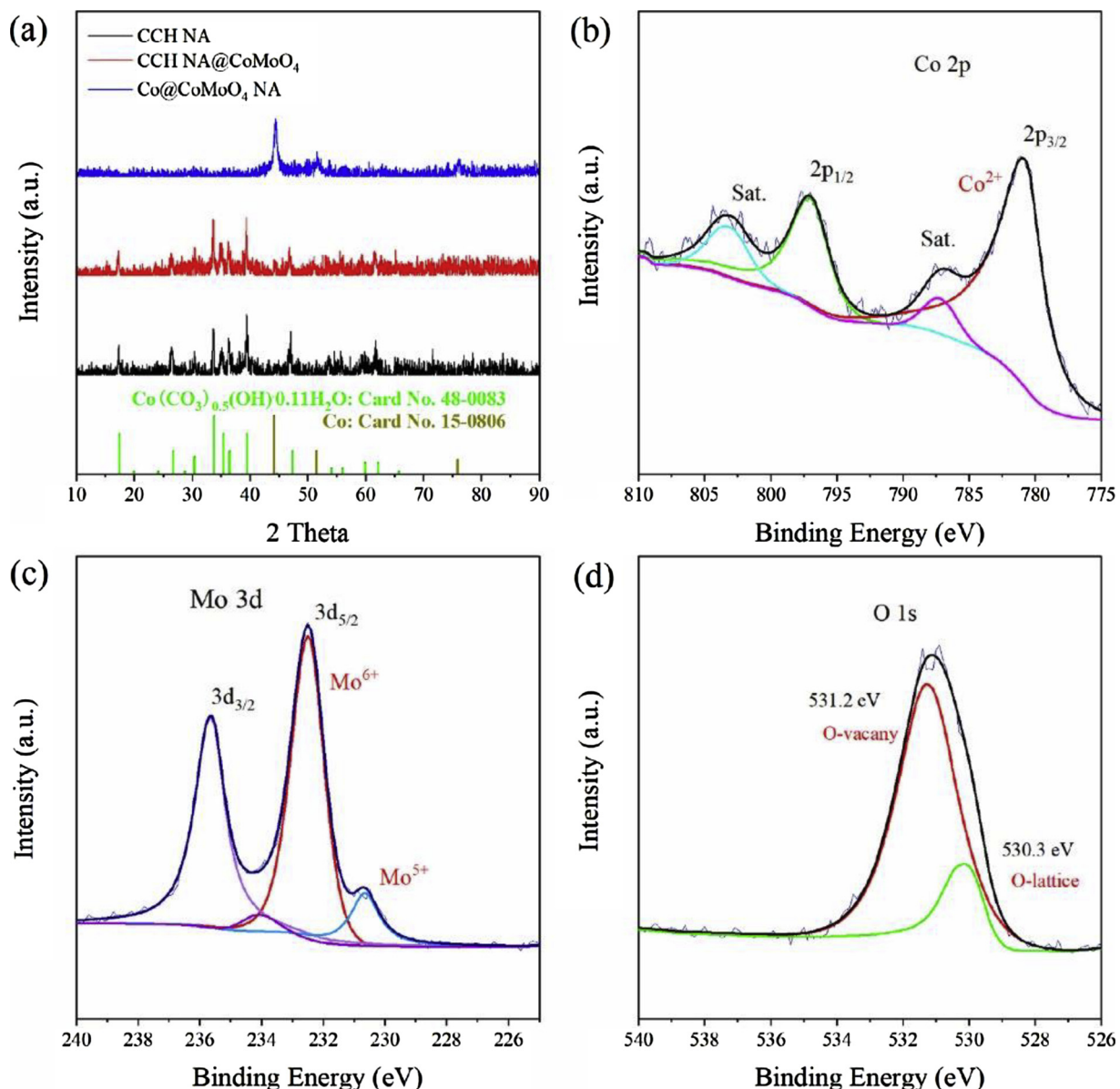


Fig. 2. (a) X-ray diffraction (XRD) pattern of CCH NA, CCH NA@CoMoO₄ and Co@CoMoO₄ NA; High resolution X-ray photoelectron spectroscopy (HR-XPS) survey spectra of Co 2p (b), Mo 3d (c) and O 1s (d).

derived from hydrogenation treatment of CCH NA shows poor activity for HER, since a large overpotential of 250 mV is required to afford 10 mA cm⁻². As another control, we synthesized CoMoO₄ nanosheets following the published procedure and annealed under the same atmosphere (H₂:N₂ = 10:90) and temperature (400 °C) as Co@CoMoO₄ NA (Figure S4). As shown in Fig. 5a, overpotential of 179 mV is recorded at 10 mA cm⁻² with CoMoO₄ nanosheets, which is also much inferior to that of Co@CoMoO₄ NA ($\eta_{10} = 46$ mV). In addition, the current density at $\eta = 250$ mV of Co@CoMoO₄ NA is 145 mA cm⁻², which is 5.2 times that of CoMoO₄ (28 mA cm⁻²). These two control experiments clearly demonstrate that neither Co nor CoMoO₄ is an efficient HER catalyst. Therefore, synergistic effect between Co and CoMoO₄ must be existed and responsible for the observed superior activity of Co@CoMoO₄ NA. It is noteworthy that a prominent reduction peak before hydrogen evolution was observed for Co@CoMoO₄ in the LSV curve, which can be assigned to the reduction of surface oxidized CoO_x species or a pseudocapacitive behavior induced by hydrogenation treatment [45]. Such background currents might result in an overestimate of activity in terms of overpotential at 10 mA cm⁻² for

Co@CoMoO₄ NA ($\eta_{10} = 46$ mV). However, as demonstrated by Faraday efficiency measurement, such reactions contribute a negligible portion to the recorded activity, since a high Faraday efficiency of 97.4% was measured (Figure S5).

Tafel slopes were extracted from the linear region of the Tafel plots according to Tafel equation: $\eta = a + b \log i$ (η is the overpotential, b is the Tafel slope, and i is the current density). As shown in Fig. 5b, Tafel slopes of 85 mV dec⁻¹, 53 mV dec⁻¹, 146 mV dec⁻¹, 152 mV dec⁻¹ and 154 mV dec⁻¹ were obtained for Co@CoMoO₄ NA, PtC, bare Ni foam, Co NA and CoMoO₄ nanosheets, respectively. This result discloses the kinetical reason that Co@CoMoO₄ NA exhibits much enhanced activity in comparison with bare Ni foam, Co NA and CoMoO₄ nanosheets. Generally, HER in basic solution follows two mechanisms, namely, the Volmer process (electrochemical hydrogen adsorption (H_{ads}): H₂O + e⁻ → H_{ads} + OH⁻) followed by either the Heyrovsky process (electrochemical desorption: H_{ads} + H₂O + e⁻ → H₂ + OH⁻) or Tafel process (chemical desorption: H_{ads} + H_{ads} → H₂) [49]. Accordingly, A Tafel slope of 120, 40, or 30 mV dec⁻¹ would be expected for different rate-determining step concerning Volmer, Heyrovsky, or Tafel step,

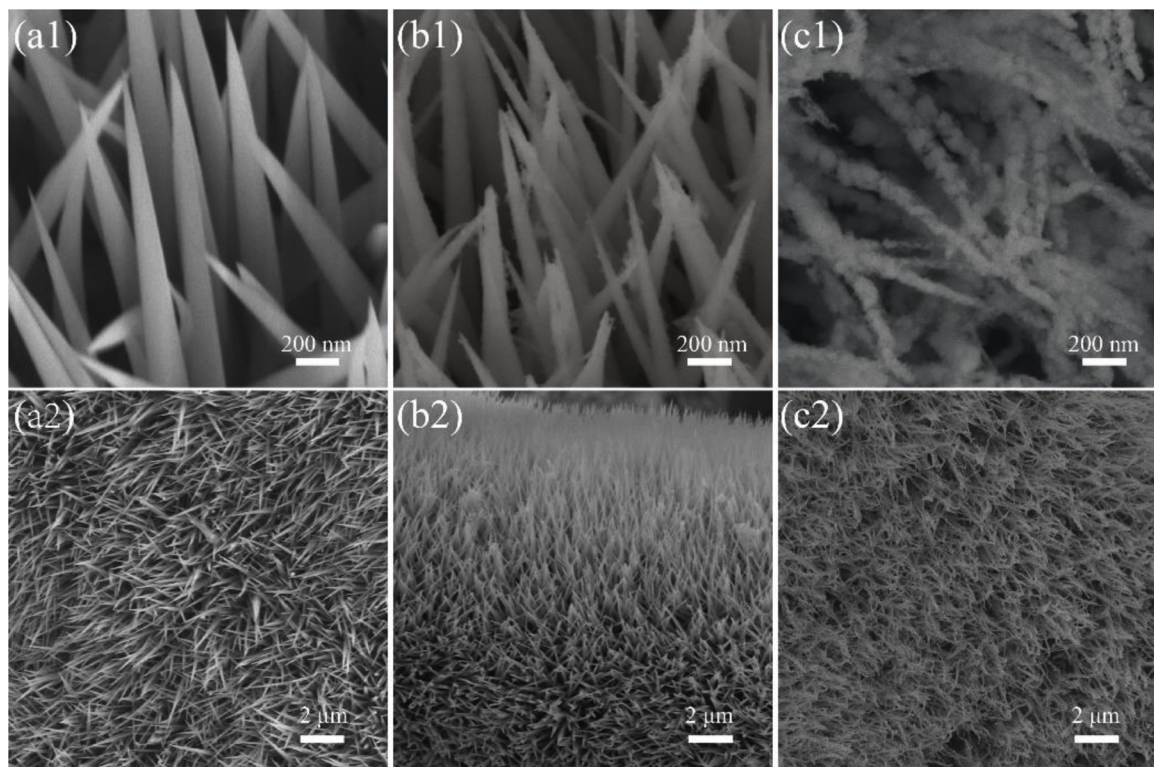


Fig. 3. Scanning electron microscopy (SEM) images of $\text{Co}(\text{CO}_3)_{0.5}(\text{OH}) \cdot 0.11\text{H}_2\text{O}$ nanowires arrays (CCH NA) (a1, a2), CCH NA@CoMoO₄ (b1, b2) and Co@CoMoO₄ NA (c1, c2) with different magnifications.

respectively [49]. Therefore, the observed Tafel slop of Co@CoMoO₄ NA demonstrates a Volmer-Heyrovsky mechanism [50].

A rational designed electrode with open porous structure is

beneficial for exposing active sites and mass transfer. Therefore, to evaluate the effective active area of catalysts, double-layer capacitances (C_{dl}) was determined by cyclic voltammetry (CV) in a non-redox

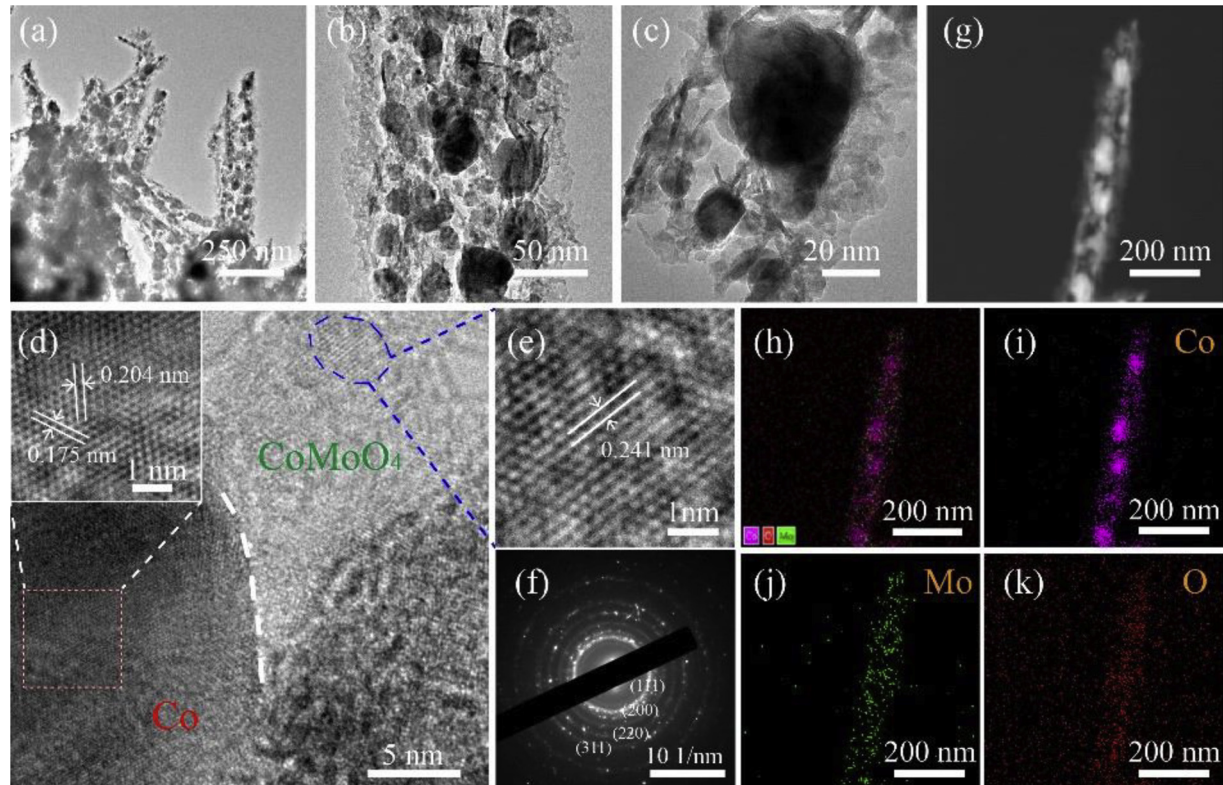


Fig. 4. TEM (a, b, c), High-resolution TEM (HR-TEM) images (d and e), selected area electron diffraction (SAED) image (f) and elemental mapping images (g–i) of Co@CoMoO₄ NA.

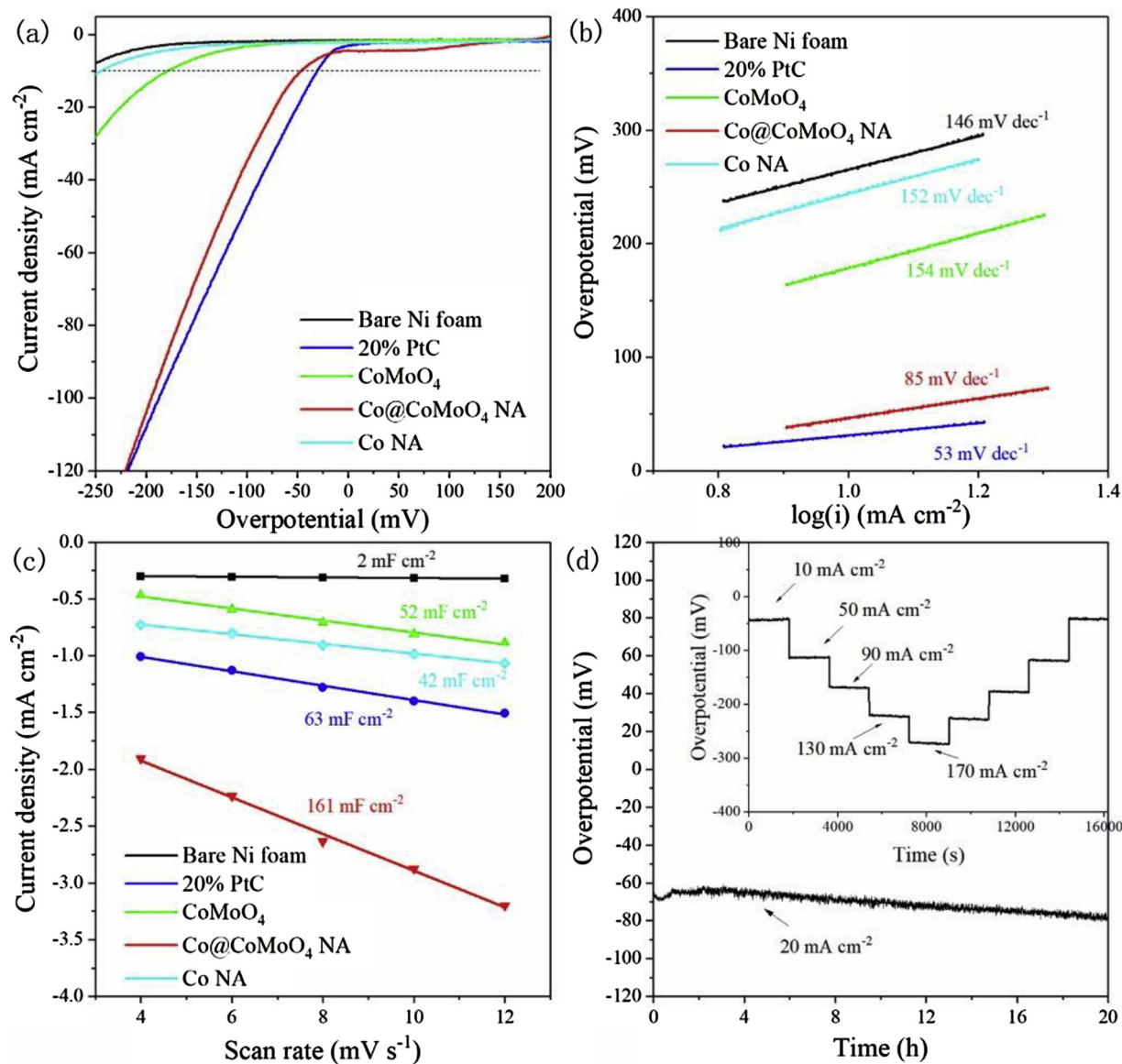


Fig. 5. (a) LSV curves and (b) Corresponding Tafel slopes of bare Ni foam (black line), 20% PtC (blue line), CoMoO₄ (green line), Co@CoMoO₄ NA (red line) and Co NA (cyan line) in 1.0 M KOH solution with a scan rate of 1 mV s^{-1} and no iR compensation; (c) Dependence of capacitive current on scan rates with bare Ni foam (black line), 20% PtC (blue line), CoMoO₄ (green line), Co@CoMoO₄ NA (red line) and Co NA (cyan line) in 1.0 M KOH solution; (d) chronopotentiometry curves of Co@CoMoO₄ NA at 20 mA cm^{-2} in 1.0 M KOH solution; inset shows the multicurrent density chronopotentiometry curves (For interpretation of the references to colour in this figure legend, the reader is referred to the web version of this article).

potential region (Figure S6) [51]. As revealed in Fig. 5c, a maximum C_{dl} value of 161 mF cm^{-2} for Co@CoMoO₄ NA was extracted by plotting the current density versus scan rate, which is nearly 3 times higher than PtC (63 mF cm^{-2}), Co NA (42 mF cm^{-2}) and CoMoO₄ (52 mF cm^{-2}). This corroborates our design concept that the CoMoO₄ species not only serve as catalyst for HER, but also function as stabilizer for maintaining an open porous electrode structure. Benefiting from this electrode design, more active sites of Co@CoMoO₄ NA are exposed to electrolyte and take part in the catalytic reaction. Electrochemical impedance spectra (EIS) were tested under the same overpotential of 50 mV for the catalysts mentioned above. Impressively, in Figure S7, Co@CoMoO₄ NA shows a small semicircle comparable to that of PtC in the EIS spectra, demonstrating a favorable charge transfer resistance (R_{ct}). This further highlight the advantage of the electrode design concept, concerning construction of a metal core for conductivity improvement purpose.

To assess the long-term durability of Co@CoMoO₄ NA, chronopotentiometry was conducted. As shown in Fig. 5d, only slightly increased overpotentials are found to maintain the current density of

20 mA cm^{-2} over a period of 20 h. Moreover, chronopotentiometry was also conducted at various current densities. Beginning at 10 mA cm^{-2} , overpotential rapidly levels off and remains constant for the following 30 min. Further increase the multiple current steps leads to the overpotentials persisted constantly at a higher value (Fig. 5d inset). Notably, overpotentials were retained after electrolysis at higher current densities. LSV curves were measured before and after this multiple current step electrolysis process and little difference were found (Figure S8). In addition to the electrochemical measurements mentioned above, SEM characterization demonstrate the good durability of Co@CoMoO₄ NA due to little degradation can be observed before and after stability test (Figure S9).

To get more insights into the origin of the superb activity of Co@CoMoO₄ NA, the intrinsic activity was assessed by normalization of catalytic currents with electrochemical surface area (ECSA) derived from C_{dl} [52]. In Figure S10, the same catalytic activity trend is extracted (i.e. PtC > Co@CoMoO₄ NA > CoMoO₄ > Co NA), demonstrating that Co@CoMoO₄ NA is intrinsically more active than CoMoO₄.

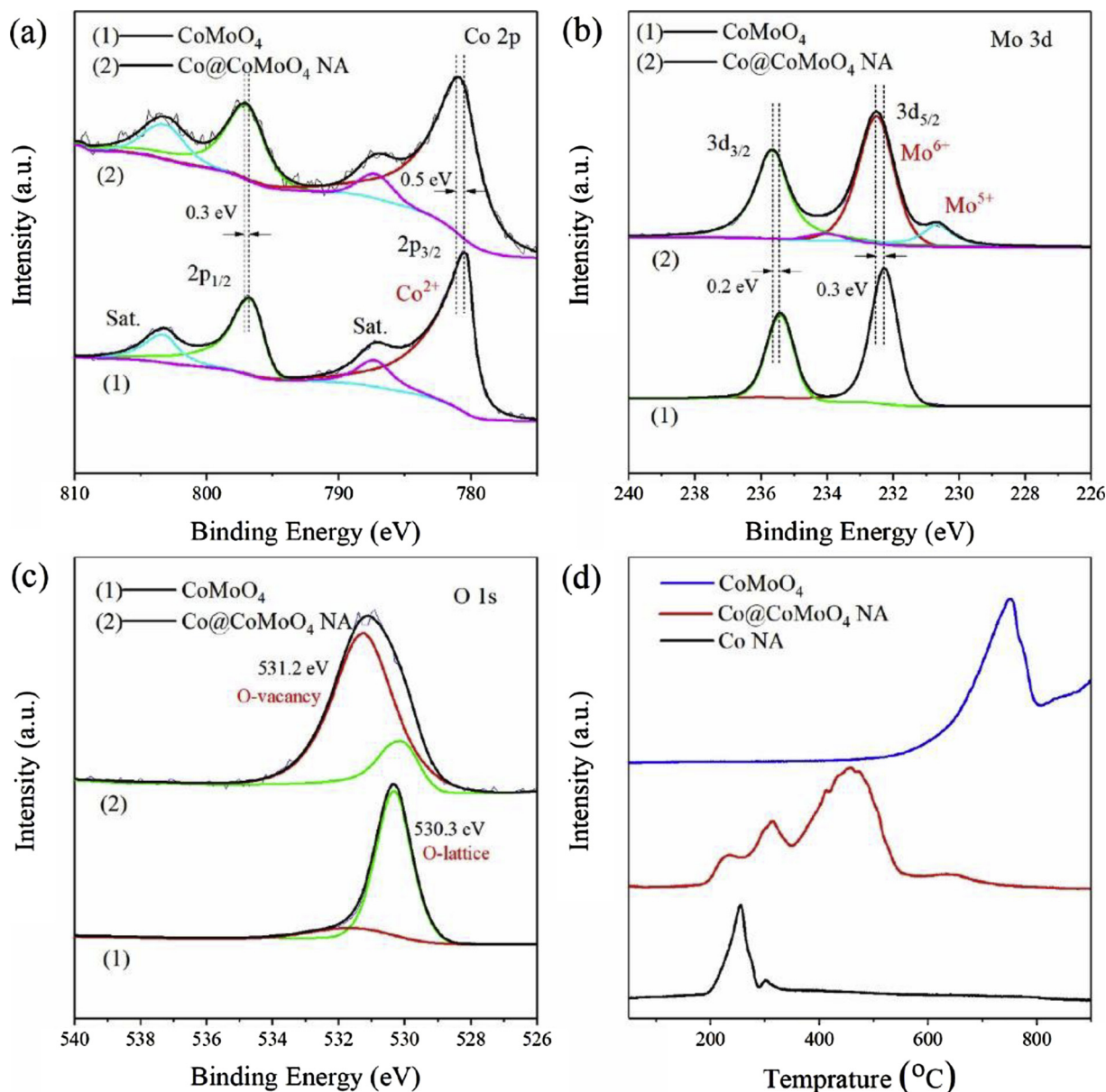


Fig. 6. (a) Co 2p, (b) Mo 3d and (c) O 1s High-resolution XPS spectra of CoMoO₄ (1) and Co@CoMoO₄ NA (2); (d) H₂-TPR curves of Co NA, CoMoO₄ and Co@CoMoO₄ NA.

and Co NA for HER. The XPS spectra of Co@CoMoO₄ NA and CoMoO₄ obtained with the same calcination protocol were recorded to disclose some evidences for the observed activity enhancement. The same elements of Co, Mo, O, C were recorded in the survey spectra (Figure S11). However, binding energies of Co 2p and Mo 3d as shown in Fig. 6a and b were found to positively shift (~0.5 eV and ~0.3 eV for Co 2p_{3/2} and Co 2p_{1/2}, respectively; ~0.3 eV and ~0.2 eV for Mo 3d_{5/2} and 3d_{3/2}, respectively), indicating a Schottky junction was possibly constructed between the metallic Co core and N-type semiconductor CoMoO₄ shell and an enhanced Lewis acidity for CoMoO₄ [53–57]. Prior researches demonstrated that the activation of H₂O (Lewis basic) can be promoted by Lewis acidic groups through Lewis acid – base interactions, thus leading to improved HER activity [58]. As a widely explored Lewis acid catalyst for methanol oxidation, mixed-metal molybdate should also be beneficial for H₂O activation through Lewis acid – base interactions [59]. The interaction between the cobalt core and CoMoO₄ shell was also evidenced by Temperature Programmed Reduction (H₂-TPR). As shown in Fig. 6d, the reduction of CoO_x species (originated by air oxidation of metallic Co) was probed at lower temperatures (200 °C ~

350 °C) [60,61], while reduction of CoMoO₄ was recorded at higher temperatures (500 °C ~ 800 °C) [62,63]. Interestingly, the reduction peaks of CoMoO₄ was found to decrease greatly (350 °C ~ 700 °C) after combining Co with CoMoO₄, indicating the strong interaction between Co and CoMoO₄ [64]. On the other hand, the O 1s spectrum of CoMoO₄ shows a major peak associated with lattice O²⁻ at binding energy of 530.3 eV [32], while a prominent peak of Co@CoMoO₄ NA belongs to O-vacancy at binding energy of 531.2 eV is illustrated in Fig. 6c [32,45,46]. Consistent with the Mo⁵⁺ species observed in Fig. 5e, more O-vacancies were introduced for Co@CoMoO₄ NA, which might be resulted from the boundary rearrangement during the reduction of CCH NA to metallic cobalt. Previous studies have demonstrated that O-vacancies are beneficial for HER [65,66].

Systematic investigations of samples obtained by calcining the CCH NA@CoMoO₄ precursor in varying temperatures (i.e. 300 °C, 400 °C, 500 °C) were carried out to get more evidences about the origin of activity enhancement. As illustrated in Fig. 7a, the catalytic activity increased with the elevating of calcination temperature first, and then falling down. The XRD patterns shown in Fig. 7e indicated a mixed

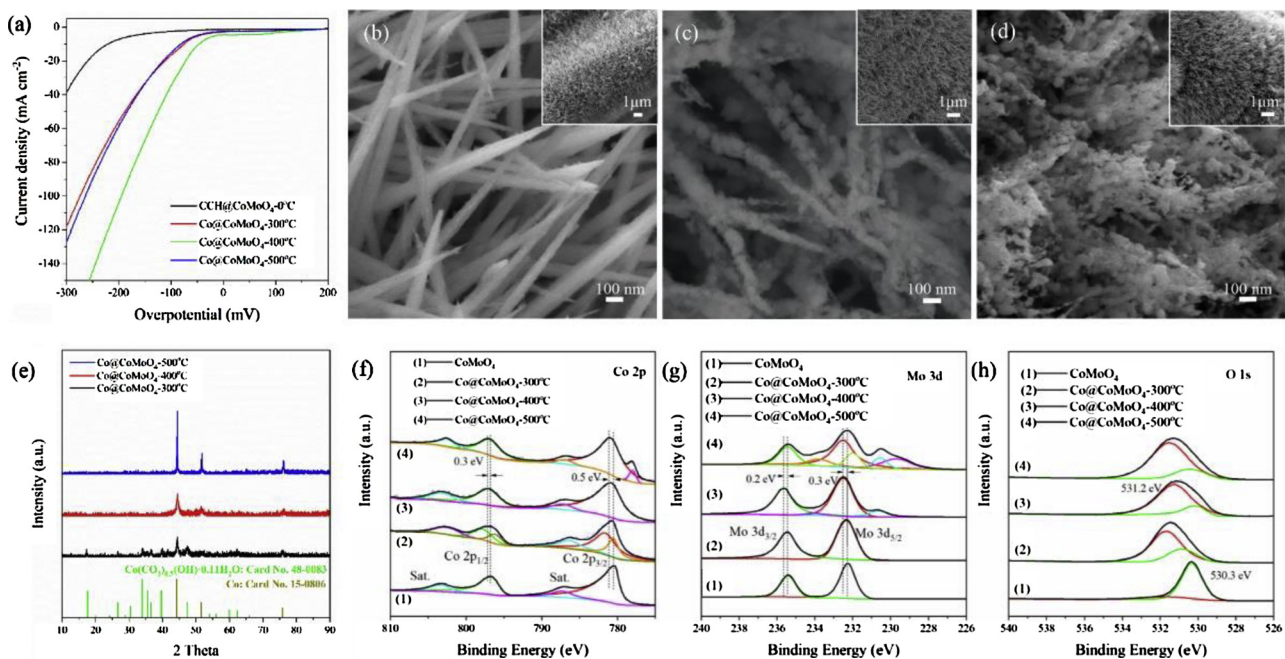


Fig. 7. (a) LSV curves of Co@CoMoO₄ calcined under 300 °C, 400 °C and 500 °C in 1.0 M KOH solution; (b) SEM image of Co@CoMoO₄-300 °C; (c) SEM image of Co@CoMoO₄-400 °C (d) SEM image of Co@CoMoO₄-500 °C; (e) XRD patterns, (f) high resolution Co 2p XPS spectra, (g) high resolution Mo 3d XPS spectra and (h) high resolution O 1s XPS spectra of Co@CoMoO₄ calcinated under 300 °C, 400 °C and 500 °C.

composition of cobalt carbonate hydroxide hydrate ($(\text{Co}(\text{CO}_3)_{0.5}(\text{OH}) \cdot 0.11\text{H}_2\text{O}$, JCPDS No. 48-0083) and cobalt (JCPDS No. 15-0806) after hydrogenation at 300 °C. Under higher temperatures, only cobalt can be detected by XRD. However, diffraction peaks with much stronger intensity can be observed for samples obtained under 500 °C, indicating a much bigger crystal size. It is not worthy that even under 500 °C, no any peaks can be indexed to Mo based compounds. This might be resulted from the relatively low loading of CoMoO₄ precursor ($\sim 0.5 \text{ mg cm}^{-2}$) as compared with CCH precursor ($\sim 4.0 \text{ mg cm}^{-2}$). Correlating the phase evolution results with the activity trend, we further deduce that synergistic effect between cobalt and CoMoO₄ plays a pivotal role as stated above.

On the other hand, XPS characterization also revealed some interesting results, which are helpful for the understanding of the improved activity. In Fig. 7f, the high-resolution Co 2p spectrum can be fitted to Co(III) and Co(II) as that of Co₃O₄, while a much higher ratio of Co(II)/Co(III) (~ 2.1) than that of pure Co₃O₄ was recorded [46]. This indicated a much more complex composition than observed by XRD. For the sample obtained under 500 °C, a new peak belonging to metallic cobalt was recorded at binding energy of 778.1 eV, this might indicate a much more shrinkage of the outer shell as mentioned above. In addition, the peaks generally show a positive shift as compared with that of bare CoMoO₄. The high-resolution Mo 3d XPS spectra were also detected. In Fig. 7g, the Mo 3d spectrum of Co@CoMoO₄-300 °C shows exactly the same character as that of bare CoMoO₄, indicating no synergistic effect exists. So, the observed activity enhancement might be attributed to the vacancies generated by hydrogenation treatment, since O 1s spectrum (Fig. 7h) shows a prominent peak corresponding to O-vacancies as discussed above. Under 500 °C, CoMoO₄ was decomposed as several new peaks corresponding to Mo (IV) and Mo (V) were detected by high-resolution Mo 3d XPS spectra [44]. Lastly, as shown in Fig. 7b-d, the nanowire arrays were fused together under 500 °C, which might also be a reason for the deteriorated performance.

Therefore, the observed superior activity for HER should be attributed to several advantage aspects including the synergistic effect between Co and CoMoO₄, O-vacancies for improved intrinsic activity and the rational designed electrode micro-structure for enhanced mass transfer and exposure of active sites.

4. Conclusion

In summary, 3D self-standing core-shell Co@CoMoO₄ NA have been successfully fabricated by hydrogenation treatment of a core-shell precursor CCH NA@CoMoO₄. When used as an integrate electrode for HER in 1.0 M KOH, magnificent catalytic activity was observed with low overpotential of 46 mV at 10 mA cm⁻², suppressing most Co based catalyst and very close to commercial PtC (31 mV at 10 cm⁻²). Electrochemical and physical characterizations demonstrated that the synergistic effect between Co and CoMoO₄ is responsible for the enhanced HER performance. Moreover, rational designed open porous architecture and the metal Co core of Co@CoMoO₄ NA was also proved to be advantageous for improved HER activity. Therefore, we believe that our study will provide new opportunities for fabricating low cost and efficient alkaline HER electro-catalysts based on multiple components interfaces modulating.

Acknowledgements

This research work was financially sponsored by National Natural Science Foundation of China (Grant No.: 21436003 and 21576032). Z. W. supervised the project. R. X., Y. D. conceived and designed the experiments. All authors discussed the results and Z. W., L. P., Y. W., C. T., and L. Z. co-wrote the paper. The authors declare no competing financial interests. Correspondence and requests for materials should be addressed to Z.W.

Appendix A. Supplementary data

Supplementary material related to this article can be found, in the online version, at doi:<https://doi.org/10.1016/j.apcatb.2019.01.035>.

References

- [1] Y. Shi, B. Zhang, Chem. Soc. Rev. 45 (2016) 1529–1541.
- [2] P. Cai, J. Huang, J. Chen, Z. Wen, Angew. Chem. Int. Ed. 56 (2017) 4858–4861.
- [3] X. Zou, Y. Zhang, Chem. Soc. Rev. 44 (2015) 5148–5180.
- [4] J. Chi, H. Yu, Chin. J. Catal. 39 (2018) 390–394.
- [5] G. Wang, J. Chen, Y. Li, J. Jia, P. Cai, Z. Wen, Chem. Commun. 54 (2018)

- 2603–2606.
- [6] P. Cai, Y. Li, G. Wang, Z. Wen, *Angew. Chem. Int. Ed.* 57 (2018) 3910–3915.
- [7] S. Anantharaj, S.R. Ede, K. Sakthikumar, K. Karthick, S. Mishra, S. Kundu, *ACS Catal.* 6 (2016) 8069–8097.
- [8] T. Wang, H. Xie, M. Chen, A. D'Aloia, J. Cho, G. Wu, Q. Li, *Nano Energy* 42 (2017) 69–89.
- [9] Y. Huang, J. Ge, J. Hu, J. Zhang, J. Hao, Y. Wei, *Adv. Energy Mater.* 8 (2018) 1701601.
- [10] Y.Y. Chen, Y. Zhang, W.J. Jiang, X. Zhang, Z. Dai, L.J. Wan, J.S. Hu, *ACS Nano* 10 (2016) 8851–8860.
- [11] S. Jing, L. Zhang, L. Luo, J. Lu, S. Yin, P.K. Shen, P. Tsakarais, *Appl. Catal. B: Environ.* 224 (2018) 533–540.
- [12] J. Tian, Q. Liu, N. Cheng, A.M. Asiri, X. Sun, *Angew. Chem. Int. Ed. Engl.* 53 (2014) 9577–9581.
- [13] J.X. Feng, J.Q. Wu, Y.X. Tong, G.R. Li, *J. Am. Chem. Soc.* 140 (2018) 610–617.
- [14] J. Liu, Y. Liu, D. Xu, Y. Zhu, W. Peng, Y. Li, F. Zhang, X. Fan, *Appl. Catal. B: Environ.* 241 (2019) 89–94.
- [15] Y. Li, K. Yin, L. Wang, X. Lu, Y. Zhang, Y. Liu, D. Yan, Y. Song, S. Luo, *Appl. Catal. B: Environ.* 239 (2018) 537–544.
- [16] A. Sivanantham, P. Ganesan, S. Shanmugam, *Adv. Funct. Mater.* 26 (2016) 4661–4672.
- [17] J. Zhang, T. Wang, P. Liu, Z. Liao, S. Liu, X. Zhuang, M. Chen, E. Zschech, X. Feng, *Nat. Commun.* 8 (2017) 15437.
- [18] Y. Xu, S. Yin, C. Li, K. Deng, H. Xue, X. Li, H. Wang, L. Wang, *J. Mater. Chem. A* 6 (2018) 1376–1381.
- [19] H. Lv, X. Chen, D. Xu, Y. Hu, H. Zheng, S.L. Suib, B. Liu, *Appl. Catal. B: Environ.* 238 (2018) 525–532.
- [20] R. Xiang, C. Tong, Y. Wang, L. Peng, Y. Nie, L. Li, X. Huang, Z. Wei, *Chin. J. Catal.* 39 (2018) 1736–1745.
- [21] K. Xu, H. Ding, M. Zhang, M. Chen, Z. Hao, L. Zhang, C. Wu, Y. Xie, *Adv. Mater.* 29 (2017).
- [22] Z. Wang, H. Liu, R. Ge, X. Ren, J. Ren, D. Yang, L. Zhang, X. Sun, *ACS Catal.* 8 (2018) 2236–2241.
- [23] P. Guo, J. Wu, X.-B. Li, J. Luo, W.-M. Lau, H. Liu, X.-L. Sun, L.-M. Liu, *Nano Energy* 47 (2018) 96–104.
- [24] W. Li, X. Gao, D. Xiong, F. Wei, W.-G. Song, J. Xu, L. Liu, *Adv. Energy Mater.* 7 (2017) 1602579.
- [25] J. Wang, H.X. Zhong, Z.L. Wang, F.L. Meng, X.B. Zhang, *ACS Nano* 10 (2016) 2342–2348.
- [26] J. Zhao, X. Ren, H. Ma, X. Sun, Y. Zhang, T. Yan, Q. Wei, D. Wu, *ACS Sustain. Chem. Eng.* 5 (2017) 10093–10098.
- [27] J. Wang, W. Cui, Q. Liu, Z. Xing, A.M. Asiri, X. Sun, *Adv. Mater.* 28 (2016) 215–230.
- [28] L. Liu, D. Li, H. Zhao, A. Dimitrova, L. Li, Y. Fang, S. Krischok, W. Shi, Y. Lei, *Appl. Catal. B: Environ.* (2018).
- [29] M. Gong, W. Zhou, M.C. Tsai, J. Zhou, M. Guan, M.C. Lin, B. Zhang, Y. Hu, D.Y. Wang, J. Yang, S.J. Pennycook, B.J. Hwang, H. Dai, *Nat. Commun.* 5 (2014) 4695.
- [30] N. Danilovic, R. Subbaraman, D. Strmcnik, K.C. Chang, A.P. Paulikas, V.R. Stamenkovic, N.M. Markovic, *Angew. Chem. Int. Ed. Engl.* 51 (2012) 12495–12498.
- [31] L. Peng, X. Zheng, L. Li, L. Zhang, N. Yang, K. Xiong, H. Chen, J. Li, Z. Wei, *Appl. Catal. B: Environ.* 245 (2019) 122–129.
- [32] X. Yan, L. Tian, S. Atkins, Y. Liu, J. Muroowich, X. Chen, *ACS Sustain. Chem. Eng.* 4 (2016) 3743–3749.
- [33] Y.Y. Chen, Y. Zhang, X. Zhang, T. Tang, H. Luo, S. Niu, Z.H. Dai, L.J. Wan, J.S. Hu, *Adv. Mater.* 29 (2017).
- [34] M. Fang, G. Dong, R. Wei, J.C. Ho, *Adv. Energy Mater.* 7 (2017) 1700559.
- [35] Y. Li, K. Yin, L. Wang, X. Lu, Y. Zhang, Y. Liu, D. Yan, Y. Song, S. Luo, *Appl. Catal. B: Environ.* 239 (2018) 537–544.
- [36] Y. Wang, J. Cai, M. Wu, J. Chen, W. Zhao, Y. Tian, T. Ding, J. Zhang, Z. Jiang, X. Li, *Appl. Catal. B: Environ.* 239 (2018) 398–407.
- [37] M.-Q. Yang, J. Wang, H. Wu, G.W. Ho, *Small* 14 (2018) 1703323.
- [38] J. Cui, X. Zhang, L. Tong, J. Luo, Y. Wang, Y. Zhang, K. Xie, Y. Wu, J. Mater. Chem. A 3 (2015) 10425–10431.
- [39] Y. Wang, W. Ding, S. Chen, Y. Nie, K. Xiong, Z. Wei, *Chem. Commun.* 50 (2014) 15529–15532.
- [40] X. Cui, X. Chen, W. Zhang, X. Yan, M. Wang, J. Lian, Z. Zheng, H. Deng, *J. Alloys. Compd.* 695 (2017) 2109–2116.
- [41] A. Sivanantham, P. Ganesan, S. Shanmugam, *Appl. Catal. B: Environ.* 237 (2018) 1148–1159.
- [42] A. Sivanantham, P. Ganesan, L. Estevez, B.P. McGrail, R.K. Motkuri, S. Shanmugam, *Adv. Energy Mater.* 8 (2018) 1702838.
- [43] Y.Y. Chen, Y. Zhang, X. Zhang, T. Tang, H. Luo, S. Niu, Z.H. Dai, L.J. Wan, J.S. Hu, *Adv. Mater.* 29 (2017).
- [44] N.S. McIntyre, D.D. Johnston, L.L. Coatsworth, R.D. Davidson, J.R. Brown, *Surf. Interface Anal.* 15 (1990) 265–272.
- [45] X. Yan, L. Tian, M. He, X. Chen, *Nano Lett.* 15 (2015) 6015–6021.
- [46] C. Zhao, B. Yongmin, H. Enyuan, L. Wen, D. Nico, T. Yang, L. Xiaolin, K. Yun, L. Yaping, Y. Xiao-Qing, W. Hailiang, S. Xiaoming, *Adv. Energy Mater.* 8 (2018) 1701694.
- [47] J.X. Feng, H. Xu, Y.T. Dong, X.F. Lu, Y.X. Tong, G.R. Li, *Angew. Chem. Int. Ed. Engl.* 56 (2017) 2960–2964.
- [48] Q. Jin, B. Ren, D. Li, H. Cui, C. Wang, *Nano Energy* 49 (2018) 14–22.
- [49] B.E. Conway, B.V. Tilak, *Electrochim. Acta* 47 (2002) 3571–3594.
- [50] Y. Zhang, X. Xia, X. Cao, B. Zhang, N.H. Tiep, H. He, S. Chen, Y. Huang, H.J. Fan, *Adv. Energy Mater.* 7 (2017) 1700220.
- [51] L.M. Da Silva, L.A. De Faria, J.F.C. Boodts, *Electrochim. Acta* 47 (2001) 395–403.
- [52] Y. Yang, W. Zhang, Y. Xiao, Z. Shi, X. Cao, Y. Tang, Q. Gao, *Appl. Catal. B: Environ.* 242 (2019) 132–139.
- [53] Z. Wu, Z. Wang, F. Geng, *ACS Appl. Mater. Interfaces* 10 (2018) 8585–8593.
- [54] J. Zhang, T. Wang, D. Pohl, B. Rellinghaus, R. Dong, S. Liu, X. Zhuang, X. Feng, *Angew. Chem. Int. Ed. Engl.* 55 (2016) 6702–6707.
- [55] Z. Wu, Z. Wang, F. Geng, *ACS Appl. Mater. Interfaces* 10 (2018) 8585–8593.
- [56] Z. Zhuang, Y. Li, Z. Li, F. Lv, Z. Lang, K. Zhao, L. Zhou, L. Moskaleva, S. Guo, L. Mai, *Angew. Chem. Int. Ed.* 57 (2018) 496–500.
- [57] B. Long, H. Yang, M. Li, M.-S. Balogun, W. Mai, G. Ouyang, Y. Tong, P. Tsakarais, S. Song, *Appl. Catal. B: Environmental* 243 (2019) 365–372.
- [58] Y.F. Xu, M.R. Gao, Y.R. Zheng, J. Jiang, S.H. Yu, *Angew. Chem. Int. Ed. Engl.* 52 (2013) 8546–8550.
- [59] K.-a. Thavornprasert, M. Capron, L. Jalowiecki-Duhamel, O. Gardoll, M. Trentesaux, A.-S. Mamede, G. Fang, J. Faye, N. Touati, H. Vezin, J.-L. Dubois, J.-L. Couturier, F. Dumeignil, *Appl. Catal. B: Environ.* 145 (2014) 126–135.
- [60] G. Grzybek, P. Stelmachowski, S. Gudyka, P. Indyka, Z. Sojka, N. Guillén-Hurtado, V. Rico-Pérez, A. Bueno-López, A. Kotarba, *Appl. Catal. B: Environ.* 180 (2016) 622–629.
- [61] L.F. Liotta, G. Pantaleo, G. Di Carlo, G. Marci, G. Deganello, *Appl. Catal. B: Environ.* 52 (2004) 1–10.
- [62] F.J. Méndez, O.E. Franco-López, X. Bokhimi, D.A. Solís-Casados, L. Escobar-Alarcón, T.E. Klimova, *Appl. Catal. B: Environ.* 219 (2017) 479–491.
- [63] X. Liu, X. Li, Z. Yan, *Appl. Catal. B: Environ.* 121–122 (2012) 50–56.
- [64] H. Liu, Y. Li, C. Yin, Y. Wu, Y. Chai, D. Dong, X. Li, C. Liu, *Appl. Catal. B: Environ.* 198 (2016) 493–507.
- [65] T. Zhang, M.-Y. Wu, D.-Y. Yan, J. Mao, H. Liu, W.-B. Hu, X.-W. Du, T. Ling, S.-Z. Qiao, *Nano Energy* 43 (2018) 103–109.
- [66] L. Zhu, M. Ran, H.T. Doan, M.I. M. P.A. S. Z. Wei, C.J. E., K.D. A., T. Srinivas, H. Junkai, Z. Yashan, R. Rampi, S.S. L, *Adv. Energy Mater.* 6 (2016) 1600528.